An Endogenous Nanomineral Chaperones Luminal Antigen and Peptidoglycan to Intestinal Immune Cells

Jonathan J Powell[1], **Emma Thomas-McKay**[1], **Vinay Thoree**[1], **Jack Robertson**[1], **Rachel E Hewitt**[1], **Jeremy N Skepper**[2], **Andy Brown**[3], **Juan Carlos Hernandez-Garrido**[4], **Paul A Midgley**[5], **Inmaculada Gomez-Morilla**[6], **Geoffrey W Grime**[7], **Karen J Kirkby**[7,8], **Neil A Mabbott**[9], **David S Donaldson**[9], **Ifor R Williams**[10], **Daniel Rios**[10], **Stephen E Girardin**[11], **Carolin T Haas**[1], **Sylvaine FA Bruggraber**[1], **Jon D Laman**[12,13], **Yakup Tanriver**[14], **Giovanna Lombardi**[15], **Robert Lechler**[15], **Richard P H Thompson**[1,16], and **Laetitia C Pele**[1]

[1]Medical Research Council Human Nutrition Research, Elsie Widdowson Laboratory, Fulbourn Road, Cambridge CB1 9NL, UK [2]Cambridge Advanced Imaging Centre, Department of Physiology, Development and Neuroscience, Anatomy Building, University of Cambridge, Cambridge, CB2 3DY, UK [3]Institute for Materials Research, SPEME, University of Leeds, Leeds, LS2 9JT, UK [4]Departamento de Ciencia de los Materiales e Ingenieria Metalúrgica y Química Inorganica, Facultad de Ciencias. Universidad de Cádiz, Campus Universitario Rio San Pedro, Puerto Real (Cádiz) 11.510, Spain [5]Department of Materials Science and Metallurgy, 27 Charles Babbage Road, University of Cambridge, Cambridge, CB3 0FS, UK [6]Technische Universitaet Dresden, Fakultaet Maschinenwesen, Institut fuer Stroemungsmechanik, 01062 Dresden, Germany [7]Ion Beam Centre, Advanced Technology Institute, Faculty of Engineering and Physical Sciences, University of Surrey, Guilford GU2 7XH, UK [8]Institute of Cancer Sciences, The University of Manchester, 27 Palatine Road, Withington, Manchester, M20 3LJ, UK [9]The Roslin Institute and Royal (Dick) School of Veterinary Sciences, University of Edinburgh, Easter Bush, Midlothian EH25 9RG, UK [10]Department of Pathology, Emory University School of Medicine, 615 Michael Street, Atlanta, GA 30322, USA [11]Department of Laboratory Medicine and Pathobiology, 1 King's College Circle, M5S 1A8 Toronto, Canada [12]Department of Immunology, Erasmus MC, University Medical Centre and MS Centre ErasMS, Rotterdam, PO Box 2040, 3000 CA Rotterdam, The Netherlands and Department of Neuroscience/Medical Physiology, UMC

Correspondence and requests for materials should be addressed to J.J.P.

Additional information: Supplementary Information accompanies this paper at www.nature.com/naturenanotechnology.

Competing financial interests: The authors have no conflict of interests.

Groningen, The Netherland [13]Department of Neuroscience, Section Medical Physiology, University of Groningen, University Medical Center Groningen, Groningen, The Netherlands [14]Department of Internal Medicine IV and Institute of Medical Microbiology and Hygiene, University Medical Center, 79106 Freiburg, Germany [15]Immunoregulation Laboratory, MRC Centre for Transplantation, King's College London, Guys' Hospital, London SE1 9RT, UK [16]Royal College of Physicians, 11 St Andrews Place, Regent's Park, London NW1 4LE, UK

Abstract

In humans and other mammals, it is known that calcium and phosphate ions are secreted from the distal small intestine into the lumen. However, why this secretion occurs is unclear. Here, we show that the process leads to the formation of amorphous magnesium-substituted calcium phosphate nanoparticles that trap soluble macromolecules, such as bacterial peptidoglycan and orally-fed protein antigens, in the lumen and transport them to immune cells of the intestinal tissue. The macromolecule-containing nanoparticles utilize epithelial M cells to enter Peyer's patches - small areas of the intestine concentrated with particle-scavenging immune cells. In wild type mice, intestinal immune cells containing these naturally-formed nanoparticles expressed the immune tolerance-associated molecule 'programmed death-ligand 1 (PD-L1)', whereas in NOD1/2 double knock-out mice, which cannot recognize peptidoglycan, PD-L1 was undetected. Our results explain a role for constitutively formed calcium phosphate nanoparticles in the gut lumen and how this helps to shape intestinal immune homeostasis.

The active secretion of calcium by the gut is often referred to as the endogenous losses but why this should occur is not known as it contributes little to the homeostasis of calcium- its excretion being mediated through urine. Phosphate ions also flux between intestinal tissue and the lumen, so calcium phosphate precipitation may ensue[1].These precipitates have not been thoroughly studied although a role in sequestration of bile acids and other colonic toxins has been proposed[1]. We have previously hypothesised that this process allows micrometre sized particles of calcium phosphate to form, which then adsorb other luminal components and carry them to phagocytic cells of intestinal tissue[1-3]. Herein we report the actual process: we show that, in fact, the endogenous luminal precipitates of mineralised calcium are abundant porous nanoparticles that appear to incorporate soluble molecules of the gut lumen and we present evidence for this process regulating the expression of cell surface PD-L1 on antigen presenting cells (APCs) in the sub-epithelial region of Peyer's patches. PD-L1 is a cell surface immuno-inhibitory molecule that co-regulates T lymphocyte function and, especially, promotes immune tolerance.

Endogenous nanomineral of the intestinal lumen

Distal small intestinal contents, recovered from ileostomy patients, were air dried on plastic-coated stubs for scanning electron microscopy (SEM). Extensive numbers of sub-micrometre sized particles were identified (Fig. 1a-b). Their calcium and phosphorus rich elemental composition was confirmed by X-ray microanalysis (XRMA) and, repeatedly, magnesium was also present (Fig. 1c). High magnification SEM indicated that the particles were generally agglomerates of smaller, nanoparticulate structures (Fig. 1b).

To avoid drying, and to better mimic *in situ* dispersion, whole cross-sections of non-aqueous resin embedded murine distal small bowel were then studied and transmission electron microscopy (TEM) was used to provide greater resolution. A large quantity of relatively electron dense nanoparticles was similarly visible (Fig. 1d) and these were again calcium (Ca) and phosphorus (P) rich by analysis with concomitant detectable magnesium (Mg) (Fig. 1e and Supplementary Fig. 1). High power TEM imaging suggested that discrete particles were amorphous and porous in structure and ~100 nm (typically 75-150 nm) in diameter (Fig. 1f and Supplementary Fig. 1). Selected area electron diffraction confirmed the lack of crystallinity (Inset Fig. 1f). Although our observations imply that endogenous nanomineral particles occur in enormous numbers in the intestinal lumen, this enumeration exceeds current analytical capabilities. Median calcium concentration is 4.2 mM[4], in 1L/24h of *succus entericus* (intestinal juice) of the human ileum, and a third of this calcium may precipitate[5]. Assuming a P:(Ca+Mg) molar ratio and packing density similar to octacalcium phosphate (because the former is variable and the latter is unknown for amorphous calcium phosphate), an average 100 nm diameter spherical particle and an estimated 50% void volume (porosity), we calculated that $\sim 2 \times 10^{14}$ luminal nanomineral particles/day will be present. This abundant endogenous nanomineral of amorphous magnesium-substituted calcium phosphate (AMCP) has not been previously observed or characterised, probably because standard processing techniques for microscopy and analysis would either dissolve the mineral or force agglomeration. Careful non-aqueous processing, however, reveals the disperse structures.

Gut immune cells acquire the endogenous luminal nanomineral

Non biological particles of ~20-250 nm diameter are known to efficiently cross the epithelial barrier of intestinal lymphoid follicles, notably the Peyer's patches of the small intestine, and may accumulate in the underlying antigen presenting cells (APCs)[3]. We therefore studied frozen sections of both human and murine Peyer's patches by light microscopy. Modified Von Kossa staining for mineralised phosphate revealed large numbers of positive cells within the sub-epithelial dome (Supplementary Fig. 2). Fluorescent calcein staining for mineralised calcium confirmed these observations (Fig. 2a-b) and demonstrated lysosomal localisation of the nanomineral (Supplementary Movie 1). A detector for back scattered electrons fitted to the SEM allowed the identification of regions with high elemental contrast in the same sub-epithelial dome area and the presence of calcium, phosphorus and magnesium were confirmed by X-ray microanalysis (Fig. 2c). Both human and murine tissue samples were similarly positive for these features.

Fluorescently labelled antibodies were then used to confirm an APC phenotype of these mineral-positive cells in murine and human Peyer's patches. We noted that artefactual staining could occur for these cells, presumably through adsorption of the labelled antibody to the intracellular mineral. Hence, we were careful to ensure that, for phenotyping, all stains showed cellular distributions typical of the anticipated antigen location and not simply coincidental with the cellular areas rich in mineral. In addition to the nuclear stain we therefore only used double staining, namely calcein for the mineral plus one phenotypic marker at a time. The majority of human and murine calcein-positive cells were strongly positive for typical cell surface markers on dendritic cells residing in the Peyer's patch sub-

epithelial dome[6,7], namely: CD11b, CD11c and HLA-DR (Fig 2d-r). A distinct sub-population was also CD68^{high} consistent with a mature macrophage phenotype (Fig. 2n and r). As expected in the gut the peripheral monocyte marker, CD14, was absent. Thus, overall, the mineral-positive cells of the Peyer's patch sub-epithelial dome were phenotypically APCs.

Imaging with TEM and scanning transmission electron microscopy (STEM) revealed that the individual AMCP nanomineral structures in sub-epithelial dome APCs (Fig. 3a-b) were porous (Fig. 3a), and often clustered possibly due to adhesion to internal vesicle membranes as this is well known for nanominerals in cell lysosomes[3]. Moreover, the particles were of similar shape, electron density and amorphous appearance to their luminal counterparts but generally appeared smaller (e.g. Fig. 3a versus Fig. 1f) indicating, perhaps, partial intracellular degradation. Apparent similarities in composition by imaging were confirmed analytically for Ca, Mg and P content, using standardless elemental quantification of X-ray microanalysis spectra from similar thin sections of Peyer's patches and luminal contents (Fig. 3c).

This tendency for intracellular clustering of AMCP nanomineral particles facilitated tomographic 3-D imaging. A large intracellular cluster was identified and imaged using high angle annular dark field (HAADF) STEM to enable sufficient contrast with unstained non-aqueous-resin-embedded specimens (Fig. 3d). A tilt series was recorded and reconstructed in three dimensions which demonstrated particles of markedly varying sizes (Fig. 3e and Supplementary Movie 2), consistent with intracellular AMCP nanomineral at differing stages of dissolution. Taken together the data above suggested that luminally formed nanomineral tracks to Peyer's patch APCs and we sought to confirm this with three specific investigations.

The first study involved dietary manipulation of the main nanomineral elements. Systemic calcium and phosphate levels are tightly controlled in mammals through the large skeletal pool. In contrast, the secretion of calcium from the circulation and into the intestinal tract (i.e. endogenous losses) diminishes when animals are maintained on low calcium diets (e.g. 0.1 g Ca/kg diet for 3 weeks *versus* 5 g Ca/kg diet normally)[8]. Thus, quantitative changes to the Peyer's patch APC nanomineral, in response to dietary calcium and phosphorus deprivation, would strongly indicate a lumen-to-APC pathway since systemic and intracellular levels of these vital elements are so carefully conserved[9]. We took snap frozen Peyer's patch tissue from four groups of mice fed diets with varying levels of these elements for three weeks. Peyer's patches of all four groups revealed abundant sub-epithelial dome cells that stained normally for mineralised calcium (Supplementary Fig. 3a-b). However, X-ray microanalysis with SEM indicated that this mineralised calcium was markedly phosphate deficient for the two groups of mice ingesting the low dietary calcium and phosphorus diets (< 0.3 g/kg diet for either element: Supplementary Fig. 3c). Moreover, mineral analysis was as expected for mice ingesting diets replete in calcium and phosphorus (> 3.8 g/kg diet for either element: Supplementary Fig. 3d). Using quantitative nuclear microscopy[2] mean P:Ca ratios of 1.15 (w/w) (Fig. 3f) were identified for nanomineral of the Peyer's patch sub-epithelial dome from mice on calcium and phosphorus replete diets. However, phosphate was absent from the mineral of mice on the diets that were low in

calcium and phosphorus (Fig. 3f). The findings support a lumen-to-Peyer's patch route for the endogenous AMCP nanomineral.

The second study considered the presence of the nanomineral in Peyer's patches of mice that lacked M cells. Transport into the Peyer's patch, of other non-biological particles in the size range of the endogenous nanomineral, is a well described phenomenon and is chiefly mediated by specialist epithelial M cells[3,10]. We therefore compared the relative abundance of Peyer's patch nanomineral by confocal microscopy in villin-cre[+] RANK[FL/FL] mice where RANKL-dependent intestinal M cell differentiation is prevented by conditional deletion of RANK in the intestinal epithelium[11]. In these mice M cells were absent from the follicle-associated epithelium overlying the Peyer's patches (Fig. 4a) and calcein-stained nanomineral was faint and a rare occurrence (Fig. 4b-c). In contrast, in matched control mice with functional RANKL-RANK signalling (i.e. RANK[FL/FL] mice) M cells were abundant (Fig. 4a) and calcein staining was normal (Fig. 4b-c).

Finally, we determined the AMCP nanomineral status of murine lymphoid structures from the large intestine. Forming a blind end tract off the caecum is the appendix, where luminal contents may reside for long periods and there is also a very large area of caecal patch. However, hyper-exposure of caecal patch immune cells to luminal contents is probably averted through regulation of M cell maturation[12]: as such the Peyer's patch and the caecal patch are very similar in terms of developmental processes as well as immunological structure and function[13]. Indeed, we confirmed that, just as for the Peyer's patch, calcein-detectable mineral was also observed in caecal patch sub-epithelial immune cells (Supplementary Fig. 4). In contrast, the colon appears to have little capacity for particle uptake[14]. Consistent with this, we found no evidence for calcein-detectable mineral in lymphoid follicles of the colon although often it was detected above the apical surface of the epithelium of regular mucosa and lymphoid structures (Supplementary Fig. 4), perhaps due to retention in the thick adherent mucus layer of the colon[14].

Collectively these data indicate that the endogenous intestinal AMCP nanomineral forms in the lumen and enters APCs of intestinal immune-inductive sites, namely the caecal and Peyer's patches, predominantly via epithelial M cells.

The endogenous nanomineral transports luminal macromolecules

The abundant homogenous formation of porous calcium phosphate nanomineral in the intestinal lumen, and its marked transport across M cells into lymphoid patch APCs, led us to question function. Calcium phosphates excel at trapping and carrying organic material into cells[15]. Indeed the nanomineral described here is amorphous, which contrasts with other forms of calcium phosphate in biological systems such as octacalcium pentophosphate and biological apatite[16], and this could facilitate its intracellular dissolution enabling the release of trapped organic material. In other words, a constitutive 'cargo ship' function for the endogenous intestinal nanomineral was considered whereby soluble, luminal organic macromolecules could be encapsulated and then transported to gut APCs.

A number of studies have confirmed the existence of discrete pathways for handling exogenously-derived cargo of differing origin at the subcellular level following the seminal

work of Blander and Medzhitov[17,18]. Particulate and soluble molecules are not anticipated to show co-incidental intracellular fluorescent signals unless their uptake is as a single conjugate[19-21]. Therefore, in the absence of *in vivo* imaging techniques that could track cargo-loading of single nanoparticles, and then show their transport from the intestinal lumen to Peyer's patch cells, we considered the intracellular co-incidence of the AMCP nanomineral with luminally-derived molecules in sub-epithelial APCs.

We fed BALB/c mice, maintained on a conventional diet or a calcium and phosphorus deplete diet, with Texas Red®-labelled ovalbumin or unlabelled ovalbumin, respectively. After 4 hours, the protein detected in Peyer's patches of mice on a conventional laboratory diet was almost solely compartmentalised within the AMCP nanomineral-positive APCs of the sub-epithelial dome (Fig. 5a-e). Since it remained possible that ovalbumin and the fluorochrome were cleaved during digestion, only the latter being associated with the nanomineral, we also directly stained the Peyer's patch sections for ovalbumin. Clear colocalisation was still observed, using the Huygens maximum least expected deconvolution algorithm to optimise resolution (Fig. 5f). Additionally, close but separated signals for intracellular calcein (AMCP nanomineral) and protein were observed (Fig. 5f): this should be expected if the nanomineral dissolves intra-lysosomally unmasking, and then releasing, its cargo. Similar findings were observed for mice fed ovalbumin on the calcium and phosphate deplete diet (Fig. 5g-k) even though, under these conditions, the nanomineral was calcium-rich but no longer a calcium phosphate (Supplementary Fig. 3c and Fig. 3f). Thus, endogenously formed nanoparticles of mineralised calcium appear to trap protein antigen in the gut lumen and chaperone it to Peyer's patch APCs.

Microbial associated molecular patterns (MAMPs), such as peptidoglycan, are present ubiquitously in the lumen of the distal gastrointestinal tract, including the ileum, due to turnover of the commensal microbiota. Peptidoglycan has been identified in human and rodent gut mucosa by the monoclonal antibody 2E9[22], which recognises only degraded/free peptidoglycan and not that present in whole bacteria[23]. Here, using 2E9 antibody, we showed that, just as for dietary-derived ovalbumin, bacterial-derived peptidoglycan was also compartmentalised with the AMCP nanomineral of Peyer's patch APCs again in terms of inseparable fluorescent signals and also as separate but closely adjacent signals (Pearson correlation coefficient = 0.71) (Figure. 5l-o).

Collectively the findings above pointed to role for endogenous gut nanomineral, which is functionally conserved in spite of dietary calcium and phosphate deficiency, in the selection and chaperoning of luminal macromolecules to Peyer's patch APCs. Notably, these organic macromolecules, as well as the Mg ions of AMCP, may serve to stabilise the particle in its amorphous state for the lifetime of the nanomineral[24,25].

Finally, we considered how the process described above may contribute to normal intestinal homeostasis.

Peptidoglycan potently stimulates the upregulation of the immunotolerance-associated co-regulatory molecule PD-L1 (B7-H1/CD274) on the cell surface[26]. Whether this mechanism extends to the gut is unclear because APCs are conditioned locally and, at least in terms of

pro-inflammatory signalling, are refractory to stimulation by bacterial fragments[27]. We therefore investigated the PD-L1 status of AMCP^{+} cells of murine Peyer's patches in both wild type mice and in NOD1 and NOD2 double knock out mice (NOD1/2[−/−])[28] which cannot recognise peptidoglycan. In wild type mice these cells were consistently PD-L1[high] (Fig. 6a and c). In contrast, in NOD1/2[−/−] mice, PD-L1 was undetectable on AMCP^{+} cells (Fig. 6b and d). In both wild type and NOD1/2[−/−] mice, sporadic low-moderate background PD-L1 expression was observed in the patch (Fig. 6a and b). This selective failure of PD-L1 expression in APCs of the intestinal nanomineral-antigen-peptidoglycan pathway indicates that peptidoglycan signalling must be intact to enable PD-L1 upregulation.

The intestinal immune response to orally-delivered protein involves cooperation between Peyer's patches and mesenteric lymph nodes. In particular, migration of APCs to the mesenteric lymph nodes implies functional activity (i.e. antigen presentation) and we confirmed that mesenteric lymph nodes in wild type mice had significant numbers of AMCP nanomineral^{+} cells (Fig. 6e and g). These were PD-L1[+], as in Peyer's patches, while in the NOD1/2[−/−] mice PD-L1 was again absent (Fig. 6f and h).

Collectively, these data suggest that in the absence of peptidoglycan recognition, antigen of the nanomineral pathway may be presented by APCs to T cells without the co-regulatory molecule PD-L1 and perhaps, therefore, without a tolerogenic instruction[29]. In this respect, it is interesting to note that in Crohn's disease peptidoglycan recognition is known to be compromised in many patients, mostly due to mutations in *NOD2*[30], and that the earliest signs of disease appear to overlie lymphoid follicles such as Peyer's patches[31]. Hence, whether this patient group represents the result of compromised PD-L1 expression in the nanomineral-antigen-peptidoglycan pathway should now be investigated.

Conclusions

Peyer's patch sampling of luminal contents, which will include some undigested dietary antigen, has long been recognised and is widely considered to be a form of local immunosensing and surveillance[6]. We now provide evidence that at least part of this process is mediated by an endogenous nanomineral chaperone, from lumen to APC, and that co-delivery of peptidoglycan in this pathway conditions the APC phenotype by switching on PD-L1. It is possible that MAMPs other than peptidoglycan are trapped and delivered to APCs in this fashion. However, at least for imprinting PD-L1 expression, they do not appear to signal as deficiency in NOD1 and NOD2, and hence peptidoglycan recognition, was sufficient to prevent PD-L1 expression in this pathway (Fig. 6). PD-L1 is immuno-inhibitory and is normally up-regulated during inflammation to help minimise tissue damage[29]. Failure to express PD-L1 in the intestine enhances the risk of inflammation[32,33] but especially so when non-self antigen is being expressed[34]. Thus, not only might the nanomineral pathway ensure that luminal antigen and peptidoglycan reach sub-epithelial immune cells without enzymatic degradation *en route* but, additionally, it could ensure that the very cells in receipt of exogenous non-self antigens are also the ones expressing PD-L1. An acquired PD-L1[high] phenotype, in a minority of APCs that are selected to be in sync with the surveillance of soluble luminal contents, could ensure that tolerogenic signalling towards 'harmless antigen' is not overly dominant and, for example, that immune responsiveness towards invasive

pathogens is maintained. Interestingly, the process adapts and remains fully functional under conditions of extreme dietary calcium and phosphate deficiency implying a degree of criticality in its function.

Overall, we propose that our findings explain: (a) why the Peyer's patch has such a remarkable ability for the uptake of non-biological nanoparticles in the ~20-250 nm range[35,36]; (b) how under constitutive conditions, luminal antigen and peptidoglycan can reach APCs of the Peyer's patch sub-epithelial dome without prior enzymatic degradation; (c) how the commensal microbiota can influence local APC development and potentially calibrate susceptibility to inflammatory disease and (d) why endogenous calcium losses occur into the gut lumen[37]. Our data also provide evidence for constitutive and beneficial self-assembly (i.e. without an associated scaffold) of nanoparticles in humans yielding new insights into the interplay between nutrition, gut physiology and the mucosal immune system. Finally, Peyer's patches are present at birth[6] and mineralised calcium nano-structures probably exist in breast milk[38-40]. We speculate from the findings presented here that the nanomineral in breast milk may be more than an easily-absorbed form of calcium and facilitate early gut immuno-surveillance of maternal milk-borne antigens[41].

METHODS

Tissue sampling

Human samples were from St Thomas' Hospital (London) with appropriate ethical approval. Fresh surgical human ileal tissue specimens (n=6 patients) were each about 20 mm by 20 mm in size. Samples were macroscopically normal and were the resection margins of tissue from patients undergoing surgery for Crohn's disease (n=2), large bowel carcinoma (n=2) and non Crohn's colitis (n=2). Luminal contents were provided from anonymised patients with ileostomies. Wild type (C57BL/6) murine ileal and large bowel tissues, as well as mesenteric lymph nodes, were obtained as surplus to requirement (LMB, Addenbrookes Hospital, Cambridge), or were from specific feeding studies[8] (as decribed in the text) or were matched controls for murine models (all on C57BL/6 background) described below. All tissues or tissue contents were either (i) snap frozen in liquid nitrogen-cooled isopentane and then stored, unprocessed or in OCT freezing medium (Thermo Scientific, USA), in liquid nitrogen until further use or (ii) were processed and embedded in non-aqueous resin (Quetol651™-see below), as stated in the text.

M cell deficient villin-cre[+] RANK[FL/FL] mice

Villin-cre[+], but not villin-cre[−], RANK[FL/FL] mice fail to express intestinal M cells as their differentiation is inhibited due to blockade of RANKL-RANK signalling[11]. Tissues from these mice, sustained on a normal laboratory chow diet, were studied. For whole-mount staining, Peyer's patches were dissected and fixed with BD Cytofix/Cytoperm (BD Biosciences, Oxford, UK). For analysis of M cells in tissue sections, Peyer's patches were removed and snap-frozen at the temperature of liquid nitrogen. Serial frozen sections (5 μm in thickness) or tissues were subsequently immunostained with rat anti-mouse GP2 mAb (MBL International, Woburn, MA). Following addition of primary Ab, tissues were stained with Alexa Fluor 488-conjugated anti-rat IgG Ab (Invitrogen, Paisley, UK) and

counterstained with either Alexa Fluor 647-conjugated phalloidin (Invitrogen) or DAPI. Sections were mounted in fluorescent mounting medium (Dako, Ely, UK) and examined using a Zeiss LSM710 confocal microscope (Zeiss, Welwyn Garden City, UK). Calcein staining and imaging was undertaken as below (staining and immunofluorescence) for regular wild type mice. For quantitation sections from the villin-cre[−] (M cell normal) and villin-cre[+] (M cell deficient) RANK[FL/FL] mice were sectioned, stained and imaged as blinded pairs to ensure precisely the same sample preparation and imaging parameters. Quantification of AMCP was carried out, on blinded sections, by manual selection (designation) of the sub epithelial dome area and then ImageJ open source software[42] was used to acquire the percentage area of calcein staining. Differences in the percentage area of calcein staining between the villin-cre[−] and villin-cre[+] mice were assessed by Mann-Whitney test.

NOD1 and NOD2 double deficient mice

NOD1/2 double knock out mice (NOD1/2[−/−]) were first generated and characterised in the group of Stephen Girardin (Toronto, Canada) and shipped to the Department of Pathology, Academic Medical Center, University of Amsterdam, for further study[28]. Peyer's patches and mesenteric lymph nodes were freshly dissected from animals that were surplus to requirement and that had been sustained on a standard laboratory chow diet. Tissues were snap frozen and shipped to Cambridge (MRC HNR) for sample preparation and imaging. Calcein staining and imaging was undertaken as below (staining and immunofluorescence) for regular wild type mice: sections from NOD1/2[−/−] and wild type mice were sectioned, stained and imaged in pairs to ensure precisely the same sample preparation and imaging parameters.

OVA feeding study and dietary mineral deprivation

Adult female BALB/c mice, 6-8 weeks of age, were purchased from Harlan Olac (Bicester, U.K.) and kept under specific pathogen-free conditions. To determine co-localization of ovalbumin and endogenous nanominerals, mice received either 1 mg of Texas Red®-labelled or unlabelled ovalbumin (Invitrogen, Paisley, UK), as stated in the text, dissolved in 0.2 ml phosphate buffered saline by oral gavage using a stainless steel gavage needle. Four hours later small intestines were harvested for analysis. All experimental procedures were performed in accordance with the Home Office Animals Scientific Procedures Act (1986). Detailed information of diets is in Pele *et al*, 2007 (ref [8]). Briefly, diets were formulated by Harlan-Teklad and consisted of a baseline diet (the very low Ca diet) that had a natural molar calcium:phosphate ratio of 0.3:1. Increased Ca levels in the subsequent diets were through addition of dibasic calcium phosphate ($CaHPO_4.2H_2O$) and calcium carbonate ($CaCO_3$) to achieve a calcium:phosphate ratio of 1.3:1 (i.e. normal ratios of these elements in a standard rodent non-purified diet). Final Ca levels of the diets were 0.009% for the very low, 0.05% for the low, 0.5% for the normal, and 1.5% for the high Ca diets.

Scanning electron microscopy (SEM) and elemental analysis of tissue samples

Tissue samples were cryo-sectioned on a Leica CM30505 cryostat, set at −24 °C, with a section thickness of ~10 μm. Resulting sections were air dried on to Melinex films and

subsequently attached to SEM stubs with silver dags (Agar, UK). They were carbon-coated before being placed in the SEM chamber for analysis. The samples were imaged with a Philips/FEI XL30 field emission gun (FEG) SEM using secondary or back scattered electron detectors as noted in the text. Energy Dispersive X-ray Spectroscopy (X-ray microanalysis) was carried out at 20 kV using an Oxford Instruments ATW SiLi spectrometer running their INCA software.

Transmission electron microscopy and elemental analysis

Human and murine samples were fixed in 2% acrolein in polypropylene glycol, dehydrated in ethanol and embedded in 'Quetol 651' epoxy resin. The resin was cured at 60 °C and sections were cut to 70 nm thicknesses before mounting on TEM grids. To allow the endogenous nanomineral to be easily visualised in a tissue background we avoided the use of heavy-metal contrast agents (e.g. uranyl acetate and lead citrate) leaving sections unstained. Sections were examined in a FEI CM200 FEG-TEM operating at 200 kV and fitted with an Oxford Instruments ultra-thin window energy dispersive X-ray (EDX) spectrometer and a Gatan imaging filter (GIF 200). We imaged at magnifications that would readily allow particles > 20 nm in diameter to be observed. The elemental content of visualised particles was measured in the TEM by focussed probe-EDX spectroscopy. Ca/P or [Ca(+Mg)]/P ratios were determined from the Oxford Instruments ISIS processing software using virtual standards for the Mg, Ca and P Kα X-ray peaks, monitored at a take-off angle of 20° and a specimen tilt angle of 15°. Care was taken to minimise the intensity of the incident electron beam because calcium phosphate particles are susceptible to irradiation damage by the high energy electrons; this results in significant mass loss for materials such as hydroxyapatite which can decompose to calcium oxide following prolonged exposure[43,44]. Selected area electron diffraction (SAED) was conducted using a selected area aperture of approximately 0.18 μm diameter in the image plane.

Scanning transmission electron microscopy and 3 dimensional tomography

Murine samples were fixed and embedded as above. Tomography experiments based on high-angle annular dark-field (HAADF) imaging in the scanning transmission electron microscopy (STEM) mode were performed at 200 kV on a FEI Tecnai F20 FEG-TEM tilting the sample from −42° to +70° at 2° intervals about a single axis using a Fischione 2020 ultra-high-tilt tomography holder. Using the Inspect 3D software, tilt series were aligned by cross-correlation and reconstructed using the SIRT algorithm (with 20 iterations).

Nuclear microscopy

Particle-induced X ray emission was carried out as previously described[2] using the microbeam facility of the Surrey Ion Beam Centre, Guildford UK [www.ionbeamcentre.co.uk]. The samples were mounted in the sample chamber of the nuclear microprobe at the University of Surrey Ion Beam Centre and were scanned using a beam of 3 MeV protons from a 2 MV Tandetron accelerator focused to a diameter of 1–2 μm. The average beam current varied between 100 pA and 200 pA. Induced X-rays were detected using a lithium-drifted silicon detector at a variable distance of 20–50 mm from the sample (Gresham Scientific Ltd., 80 mm^2 active area). Based upon parallel confocal microscopy observations, elemental maps ranging from 1×1 mm^2 to 100×100 μm^2, were

recorded. PIXE spectra from individual particles were recorded by positioning the beam on each particle area sequentially. Unpaired, 2-tailed student t tests were applied to assess differences between low Ca/P and high Ca/P diets.

Confocal microscopy

Work with traditional paraffin-embedded specimens indicated that endogenous nanominerals were lost and/or artefactually mobilised during processing and so all confocal microscopy was carried out on frozen sections. Peyer's patches were cryo-sectioned (Leica CM3050S) at 12 μm and collected on SuperFrost® slides (Thermo Scientific, USA) and allowed to air dry for 30 min at room temperature. Unless otherwise stated, sections were imaged with a Leica SP2 confocal microscope (Leica Microsystems, Germany) at 488, 568 or 633 nm laser lines, fitted with diode Ar/ArKr and HeNe lasers, using either a ×25 multi-immersion lens or a ×63, 1.2 NA water objective lens. Data were recorded using the Leica Confocal Software (v2.61) and images processed using the open-source ImageJ software[42]. Data were collected as 8-bit greyscale images and assigned appropriate colours subsequently: nuclei are shown grey or blue to best facilitate visualisation of the non-nuclear stains (i.e. calcein and fluorescent antibodies against ovalbumin, peptidoglycan and cell surface markers).

Staining and Immunofluorescence

Staining for endogenous nanomineral

Modified Von Kossa Staining: Sections were fixed in 10% w/v formaldehyde-PBS (Sigma) for 10 min followed by immediate washing in ultra high purity (UHP) water for 5 min. The washed sections were placed in a Coplin jar containing 1% silver nitrate solution and incubated for 1 h at room temperature, then washed in UHP water for 5 min. The sections were covered with UHP water and incubated under ultraviolet light for 1h, followed by a dip in 5% sodium thiosulphate solution for 5 min to remove the un-reacted silver. After a final wash in UHP water for 5 min, sections were counter stained with haematoxylin solution for 1 min, washed and dehydrated using three changes of IMS and cleared with three changes of xylene. The sections were coversliped using xylene based DPX.

Calcein staining: Sections were fixed in 2% formaldehyde-PBS (Sigma) for 10 min and then washed in three changes of 0.1 M Tris-HCL buffer, for 3 min each. Fixed sections were incubated with 2.5 μM calcein Tris-HCL solution in a glass coplin jar for 20 min at room temperature and with light exposure restricted to the minimum. Following incubation, the sections were washed carefully with three changes of 0.1 M Tris-HCl buffer for 3 min each.

Double staining for endogenous nanomineral and phenotypic markers—

Murine sections were fixed using 4% (w/v) formaldehyde-PBS (Sigma) for 10 min and then washed with 3 changes of Tris-buffered saline (TBS) at pH 8.2. Sections were then blocked for 2 h using 5% goat serum (PAA Laboratories, UK), 1% bovine serum albumin (Sigma), 0.3 M glycine (Sigma) and 0.1% Triton X-100 (Sigma) in TBS and washed with 3 changes of TBS. Primary antibodies for CD11c and CD11b were next applied and incubated for 1 h and 4 h respectively. Following washing with 3 changes of TBS, sections were then incubated with secondary antibodies, for 1 h, and finally washed with 3 changes of TBS.

Primary antibodies were Rat anti-mouse CD11b (M1/70) (Biolegend, USA) at 1:200 working concentration and Hamster anti-mouse CD11c (N418) (AbD Serotec, UK) at 1:100 working concentration. Secondary antibodies were Goat anti-rat IgG (H+L) Alexa Fluor® 568 (Invitrogen, UK) at 1:200 working concentration and Goat anti-hamster IgG (H+L) Alexa Fluor® 568 (Invitrogen, UK) at working concentration 1:200.

Human sections were fixed in 2% formaldehyde (4 °C, 10 min), washed with 0.1 M Tris buffer (pH 8.0) and incubated with primary antibodies for CD68, HLA-DR and CD14 for 1 h at room temperature (RT), and for CD11b and CD11c overnight at 4°C. After further washing in 0.1 M Tris buffer, the slides were then incubated with biotinylated secondary antibodies (diluted in foetal calf serum 1:250, v/v) for 1 h at RT and labelled with Alexa Fluor® 568 conjugated streptavidin to enable detection (1 h, RT). All sections (i.e. murine and human) were finally stained with calcein for endogenous nanomineral and counterstained with To-Pro 3 (Invitrogen, UK) or propidium iodide respectively. Sections were washed with three changes of TBS and permanently mounted with ProLong® gold antifade reagent (Invitrogen, UK). These cell surface antigens were all confirmed in specific, positive-control tissues that contain cells expressing these markers (namely appendix, placenta and tonsil).

Double staining for endogenous nanomineral and PD-L1—Murine sections were fixed using 4% (w/v) formaldehyde-PBS (Sigma) for 10 min and then washed with 3 changes of Tris-buffered saline (TBS) at pH 8.2. Sections were then blocked for 1 h using 10% goat serum (PAA Laboratories, UK), 1% bovine serum albumin (Sigma), 0.3 M glycine (Sigma) and 0.1% Triton X-100 (Sigma) in TBS and washed with 3 changes of TBS. The primary antibody for PD-L1 (10F.9G2) (Biolegend, USA) was next applied and incubated for 1 h. Following washing with 3 changes of TBS, sections were then incubated with Goat anti-rat IgG (H+L) Alexa Fluor® 568 (Invitrogen, UK) at 1:200 working concentration, for 1 h, and finally washed with 3 changes of TBS.

Staining for endogenous nanomineral and dietary antigen, bacterial peptidoglycan and lysozyme—Dual staining for the dietary protein ovalbumin and for endogenous nanomineral was achieved using OVA-Alex Fluor® 633 and calcein, respectively, and as described above for murine sections. Staining for bacterial peptidoglycan was achieved by using the mouse Mab 2E9 (mouse IgG3)[23]. Briefly, human sections were fixed in 2% formaldehyde (4 °C, 10 min). After three washes in Tris buffer (pH 7.4), sections were blocked in 1% BSA/Tris buffer and then incubated with biotinylated 2E9 (diluted 1:500 in Tris buffer) overnight, at 4°C. After further washing, sections were subsequently incubated with streptavidin (1:100, 30 min, RT) and with TSA (1:100, 10 min, RT). Endogenous nanomineral staining and nuclear counterstain were finally carried out as described above for sections of human tissue.

Lysosomal staining was by anti-lysozyme antibody. Sections of human Peyer's patch were fixed in 4% PFA (10 minutes), blocked with normal serum (5% goat serum, 1% BSA in PBS at pH 7.8 for 1 hour at room temperature) and incubated with mouse anti-lysozyme (Clone: [BGN/06/961]; Abcam, UK) at 1:50 dilution and 4 °C overnight. The primary antibody was detected using goat anti-mouse Alexa Fluor® 568 antibody (1:200 1 hour,

room temperature; Invitrogen, UK). AMCP nanomineral was stained with calcein (0.001M, 30 minutes, room temperature; Sigma, UK) and the nuclei stained with Hoescht 33342 (2 μg/ml, 20 minutes, room temperature).

Supplementary Material

Refer to Web version on PubMed Central for supplementary material.

Acknowledgements

REFERENCES

1. Powell JJ, Thoree V, Pele LC. Dietary microparticles and their impact on tolerance and immune responsiveness of the gastrointestinal tract. Br. J. Nutr. 2007; 98(Suppl 1):S59–63. [PubMed: 17922962]

2. Gomez-Morilla I, Thoree V, Powell JJ, Kirkby KJ, Grime GW. Identification and quantitative analysis of calcium phosphate microparticles in intestinal tissue by nuclear microscopy. Nucl. Instrum. Methods. Phys. Res. B. 2006; 249:665–669.

3. Powell JJ, Faria N, Thomas-McKay E, Pele LC. Origin and fate of dietary nanoparticles and microparticles in the gastrointestinal tract. J. Autoimmun. 2010; 34:J226–233. [PubMed: 20096538]

4. Geigy Scientific Tables. 8th edn. Vol. Vol. 1. CIBA-GEIGY Limited; Basle, Switzerland: 1981.

5. Schedl HP, Osbaldiston GW, Mills IH. Absorption, secretion, and precipitation of calcium in the small intestine of the dog. Am J Physiol. 1968; 214:814–819. [PubMed: 4966813]

6. Jung C, Hugot JP, Barreau F. Peyer's Patches: The Immune Sensors of the Intestine. Int. J. Inflam. 2010; 2010:823710. [PubMed: 21188221]

7. Mowat AM, Bain CC. Mucosal macrophages in intestinal homeostasis and inflammation. J. Innate. Immun. 2011; 3:550–564. [PubMed: 22025201]

8. Pele LC, et al. Low dietary calcium levels modulate mucosal caspase expression and increase disease activity in mice with dextran sulfate sodium induced colitis. J. Nutr. 2007; 137:2475–2480. [PubMed: 17951488]

9. Civitelli R, Ziambaras K. Calcium and phosphate homeostasis: concerted interplay of new regulators. J. Endocrinol. Invest. 2011; 34:3–7. [PubMed: 21985972]

10. Neutra MR, Kraehenbuhl JP. Transepithelial transport and mucosal defence I: the role of M cells. Trends. Cell. Biol. 1992; 2:134–138. [PubMed: 14731967]

11. Knoop KA, et al. RANKL is necessary and sufficient to initiate development of antigen-sampling M cells in the intestinal epithelium. J. Immunol. 2009; 183:5738–5747. [PubMed: 19828638]

12. Kimura S, et al. Visualization of the entire differentiation process of murine M cells: suppression of their maturation in cecal patches. Mucosal. Immunol. 2014 http://www.nature.com/mi/journal/vaop/ncurrent/full/mi201499a.html.

13. Masahata K, et al. Generation of colonic IgA-secreting cells in the caecal patch. Nat. Commun. 2014; 5:3704. [PubMed: 24718324]

14. Szentkuti L. Light microscopical observations on luminally administered dyes, dextrans, nanospheres and microspheres in the pre-epithelial mucus gel layer of the rat distal colon. J. Control. Release. 1997; 46:233–242.

15. Uskokovic V, Uskokovic DP. Nanosized hydroxyapatite and other calcium phosphates: chemistry of formation and application as drug and gene delivery agents. J. Biomed. Mater. Res B. Appl. Biomater. 2011; 96:152–191. [PubMed: 21061364]

16. Dorozhkin SV. Nanosized and nanocrystalline calcium orthophosphates. Acta. Biomater. 2010; 6:715–734. [PubMed: 19861183]

17. Blander JM, Medzhitov R. Regulation of phagosome maturation by signals from toll-like receptors. Science. 2004; 304:1014–1018. [PubMed: 15143282]

18. Blander JM, Medzhitov R. Toll-dependent selection of microbial antigens for presentation by dendritic cells. Nature. 2006; 440:808–812. [PubMed: 16489357]

19. Chong CS, et al. Enhancement of T helper type 1 immune responses against hepatitis B virus core antigen by PLGA nanoparticle vaccine delivery. J. Control. Release. 2005; 102:85–99. [PubMed: 15653136]

20. Heit A, Schmitz F, Haas T, Busch DH, Wagner H. Antigen co-encapsulated with adjuvants efficiently drive protective T cell immunity. Eur. J. Immunol. 2007; 37:2063–2074. [PubMed: 17628858]

21. Schlosser E, et al. TLR ligands and antigen need to be coencapsulated into the same biodegradable microsphere for the generation of potent cytotoxic T lymphocyte responses. Vaccine. 2008; 26:1626–1637. [PubMed: 18295941]

22. Klasen IS, et al. The presence of peptidoglycan-polysaccharide complexes in the bowel wall and the cellular responses to these complexes in Crohn's disease. Clin. Immunol. Immunopathol. 1994; 71:303–308. [PubMed: 7515336]

23. Schrijver IA, et al. Bacterial peptidoglycan and immune reactivity in the central nervous system in multiple sclerosis. Brain. 2001; 124:1544–1554. [PubMed: 11459746]

24. Boskey AL, Posner AS. Magnesium stabilization of amorphous calcium phosphate: a kinetic study. Mat. Res. Bull. 1974; 9:907–916.

25. Termine JD, Peckauskas RA, Posner AS. Calcium phosphate formation in vitro. II. Effects of environment on amorphous-crystalline transformation. Arch. Biochem. Biophys. 1970; 140:318–325. [PubMed: 4319593]

26. Hewitt RE, et al. Immuno-inhibitory PD-L1 can be induced by a peptidoglycan/NOD2 mediated pathway in primary monocytic cells and is deficient in Crohn's patients with homozygous NOD2 mutations. Clin. Immunol. 2012; 143:162–169. [PubMed: 22397822]

27. Davies JM, MacSharry J, Shanahan F. Differential regulation of Toll-like receptor signalling in spleen and Peyer's patch dendritic cells. Immunology. 2010; 131:438–448. [PubMed: 20545785]

28. Stroo I, et al. Phenotyping of Nod1/2 double deficient mice and characterization of Nod1/2 in systemic inflammation and associated renal disease. Biol. Open. 2012; 1:1239–1247. [PubMed: 23259058]

29. Francisco LM, Sage PT, Sharpe AH. The PD-1 pathway in tolerance and autoimmunity. Immunol. Rev. 2010; 236:219–242. [PubMed: 20636820]

30. van Heel DA, et al. Muramyl dipeptide and toll-like receptor sensitivity in NOD2-associated Crohn's disease. Lancet. 2005; 365:1794–1796. [PubMed: 15910952]

31. Gullberg E, Soderholm JD. Peyer's patches and M cells as potential sites of the inflammatory onset in Crohn's disease. Ann. N. Y. Acad. Sci. 2006; 1072:218–232. [PubMed: 17057202]

32. Fukaya T, et al. Crucial roles of B7-H1 and B7-DC expressed on mesenteric lymph node dendritic cells in the generation of antigen-specific CD4+Foxp3+ regulatory T cells in the establishment of oral tolerance. Blood. 2010; 116:2266–2276. [PubMed: 20574047]

33. Scandiuzzi L, et al. Tissue-expressed B7-H1 critically controls intestinal inflammation. Cell. Rep. 2014; 6:625–632. [PubMed: 24529703]

34. Reynoso ED, et al. Intestinal tolerance is converted to autoimmune enteritis upon PD-1 ligand blockade. J. Immunol. 2009; 182:2102–2112. [PubMed: 19201863]

35. Awaad A, Nakamura M, Ishimura K. Imaging of size-dependent uptake and identification of novel pathways in mouse Peyer's patches using fluorescent organosilica particles. Nanomedicine. 2012; 8:627–636. [PubMed: 21889475]

36. Sass W, Dreyer HP, Seifert J. Rapid insorption of small particles in the gut. Am. J. Gastroenterol. 1990; 85:255–260. [PubMed: 2309677]

37. Davies KM, Rafferty K, Heaney RP. Determinants of endogenous calcium entry into the gut. Am. J. Clin. Nutr. 2004; 80:919–923. [PubMed: 15447899]

38. Cross KJ, Huq NL, Palamara JE, Perich JW, Reynolds EC. Physicochemical characterization of casein phosphopeptide-amorphous calcium phosphate nanocomplexes. J. Biol. Chem. 2005; 280:15362–15369. [PubMed: 15657053]

39. de Kruif CG, Huppertz T, Urban VS, Petukhov AV. Casein micelles and their internal structure. Adv. Colloid. Interface. Sci. 2012; 171-172:36–52. [PubMed: 22381008]

40. McGann TC, et al. Amorphous calcium phosphate in casein micelles of bovine milk. Calcif. Tissue. Int. 1983; 35:821–823. [PubMed: 6652558]

41. Minniti F, et al. Breast-milk characteristics protecting against allergy. Endocr. Metab. Immune. Disord. Drug. Targets. 2014; 14:9–15. [PubMed: 24450452]

42. Schneider CA, Rasband WS, Eliceiri KW. NIH Image to ImageJ: 25 years of image analysis. Nat. Methods. 2012; 9:671–675. [PubMed: 22930834]

43. Bilton, M.; Brown, AP.; Milne, SJ. Investigating the optimum conditions for the formation of calcium oxide, used for CO2 sequestration, by thermal decomposition of calcium acetate. Electron Microscopy and Analysis Group Conference 2011 (Emag 2011); 2012. 371

44. Bres EF, Hutchison JL, Senger B, Voegel JC, Frank RM. HREM study of irradiation damage in human dental enamel crystals. Ultramicroscopy. 1991; 35:305–322. [PubMed: 1656575]
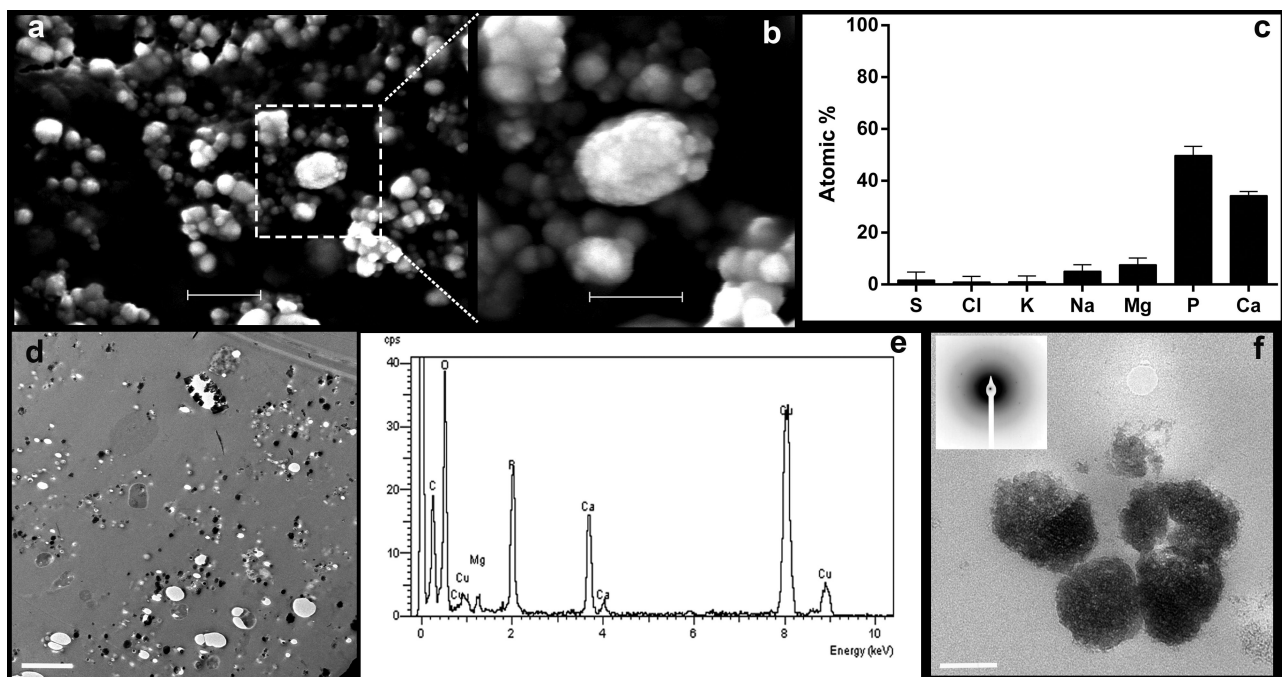
Figure 1. Characterisation of endogenous mineral of the intestinal lumen
Distal small bowel contents from humans (**a-c**) and mice (**d-f**) visualised by electron microscopy (EM) and analysed for elemental composition (**c and e**) and crystallographic phase (**f** inset). **a, b** – SEM at low (**a**; scale bar, 1 μm) and high (**b**; scale bar, 500 nm) magnification with standardless X-ray microanalysis (**c**) of 11 separate particle regions (mean + SD). **d, f** – TEM at low (**d**; scale bar, 2 μm) and high (**f**; scale bar, 100 nm) magnification. Inset **f** – Selected area electron diffraction demonstrated the absence of any significant crystallinity. **e** – A typical energy dispersive X-ray microanalysis spectrum showing the elemental composition of an endogenous mineral particle (note the Cu signal is generated by the TEM specimen support grid and the C by the embedding resin).
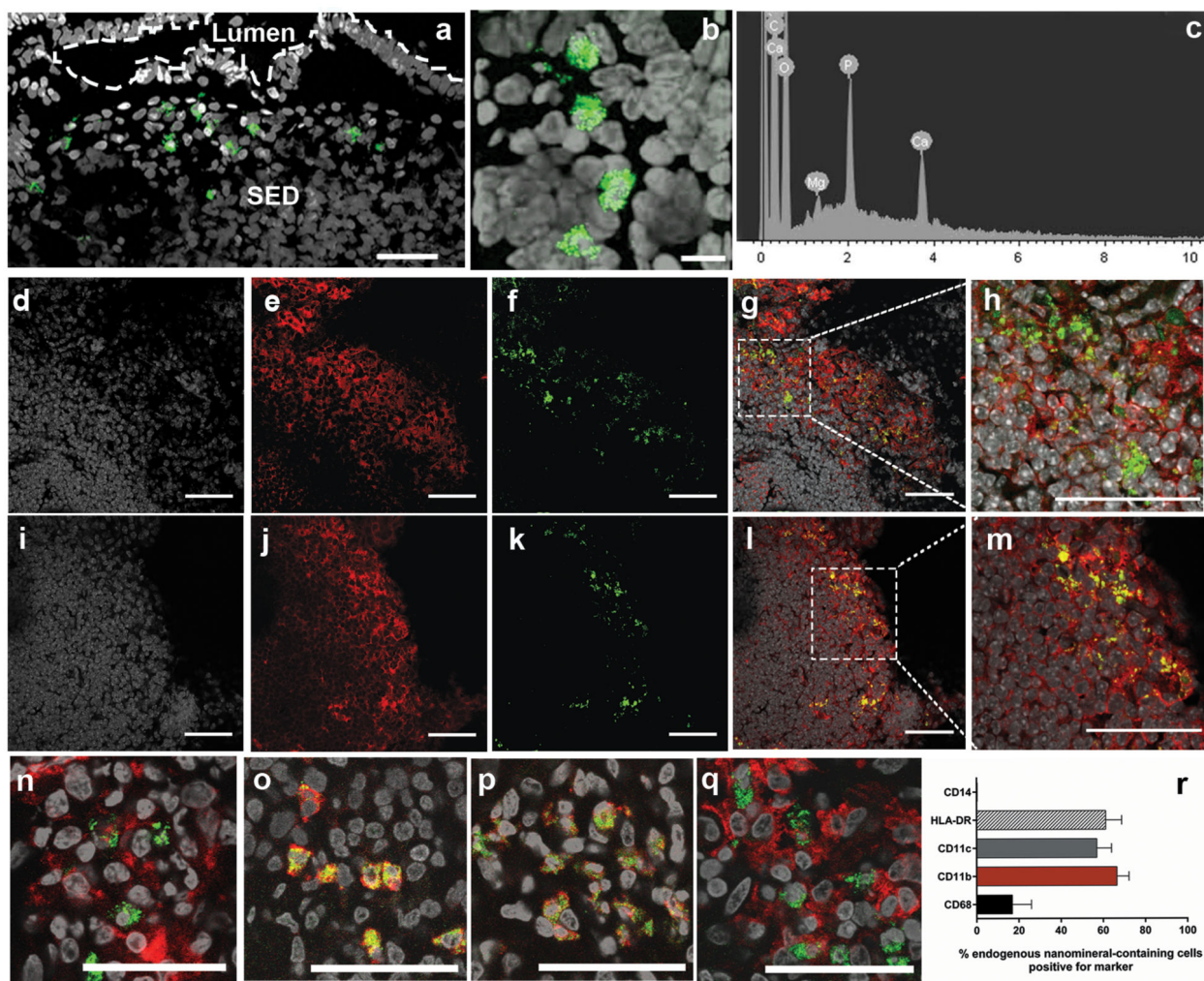
Figure 2. Phenotypic and nanomineral characterisation of sub-epithelial dome (SED) cells in murine and human Peyer's patches (PP)

a – Human PP SED stained for nuclei by propidium iodide (grey) and for mineralised calcium by calcein (green) and visualised by confocal microscopy. The gap between the epithelial cells (delineated apically by the broken white line) and cells of the SED is a consequence of frozen sectioning. Scale bar, 50 μm. **b** – The punctate nature of the stained mineral, shown from higher resolution 3D reconstructed confocal images, is consistent with localisation to distinct intracellular vesicles. Scale bar, 20 μm. **c** –Typical energy dispersive X-ray microanalysis of the mineral. **d-m**- Confocal micrographs of mouse SED stained with To-Pro-3 for nuclei (grey, images d and i), plus either anti-CD11b (red; image e) or anti-CD11c (red, images j), and calcein for endogenous mineral (green, images f and k). Overlay images in g and l confirms an APC phenotype (i.e. CD11b$^+$ and Cd11c$^+$) of the calcein$^+$ cells. Scale bars, 50 μm. **n-r** – Phenotype of the calcein$^+$ cells (green) of the SED in humans: **n-q** shows representative staining for CD68 (red), CD11b (red), CD11c (red) and HLA-DR (red), respectively. Scale bars; 50 μm. **r** – % calcein$^+$ cells that express these markers (n = 6) again confirming an APC phenotype for these cells.
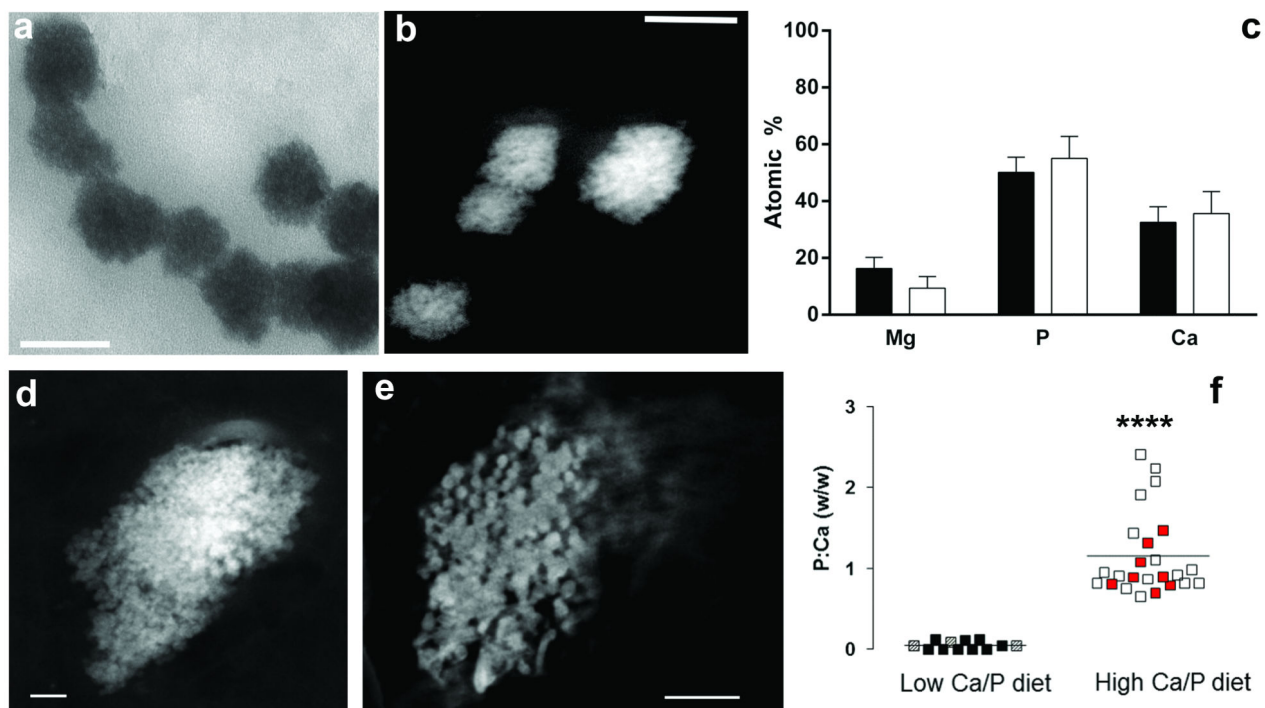
Figure 3. EM characterisation of murine endogenous nanomineral and 3D nanotomography
a – Examples by bright field TEM and **b** – HAADF STEM imaging of clusters of endogenous nanomineral within cells of the Peyer's patch (PP) sub-epithelial dome (SED). Scale bar, 100 nm. **c** –Calcium, magnesium and phosphorus composition of endogenous nanomineral in PP SED (n = 20 separate regions, black) or the murine intestinal lumen (n = 22 separate regions, white), by standardless X-ray microanalysis, Mean + SD. **d** – A large cluster was imaged by HAADF STEM and **e** – a tilt series was reconstructed for 3D visualisation; XY orthoslice from the 3D reconstruction where particles and internal porosity are observed. Scale bars, 100 nm and 200 nm, respectively. **f** – Quantitative P:Ca ratios of the nanomineral of the SED by nuclear microscopy for mice on low (grey squares) and very low (black squares) Ca and P diets versus those on normal (open squares) or high (red squares) Ca and P diets. Horizontal bars represent the mean for each group. **** p< 0.0001 versus grey/black, Mann-Whitney test.
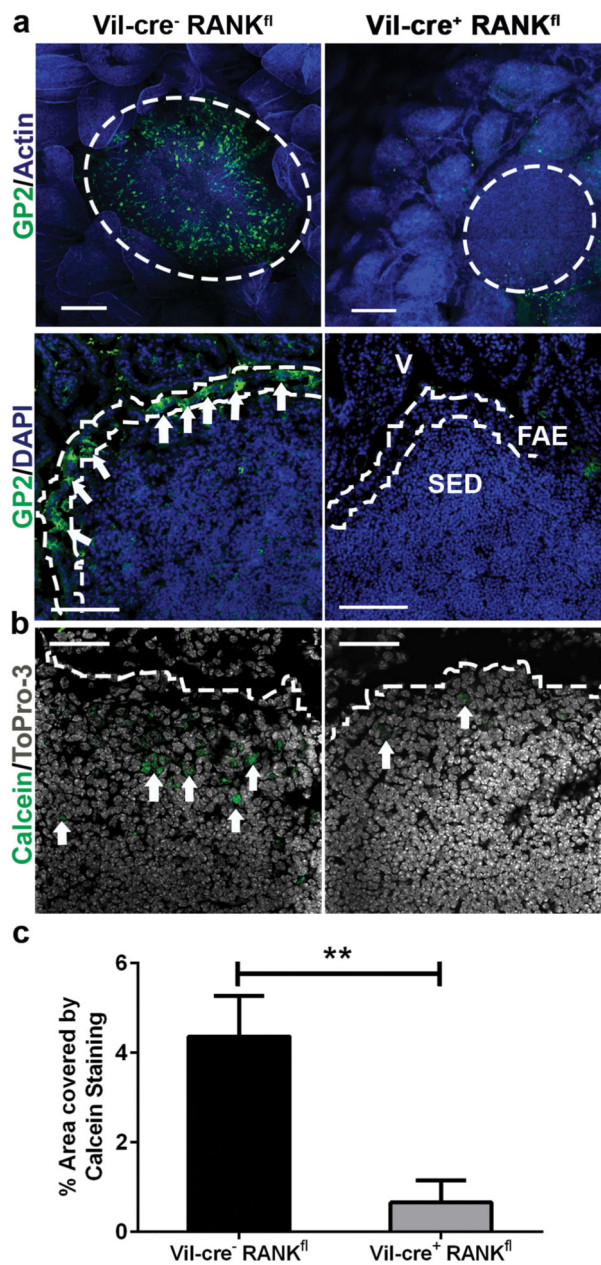
Figure 4. AMCP nanomineral uptake from the gut lumen into Peyer's patches is substantially impeded in the absence of M cells in the follicle associated epithelium

a – Upper panels. Whole-mount immunohistochemistry showing that GP2-expressing M cells (green, arrows in lower panels) are absent in the follicle associated epithelium (FAE) of villin-cre+ RANKL$^{FL/FL}$ mice (right-hand panels) when compared to villin-cre− RANKL$^{FL/FL}$ control mice (left-hand panels). Tissues are counterstained to detect F-actin (blue). Scale bars, 200 μm. Lower panels show immunohistochemistry analysis of frozen sections of Peyer's patches from the same mice. Sections are counterstained with DAPI to detect cell nuclei (blue). Scale bars, 100 μm. Dashed lines indicate the boundary of the FAE. SED, sub-epithelial dome; V, villi. **b** – Calcein staining (green) for mineralised calcium

(white arrows) in villin-cre[+] RANKL[FL/FL] mice (right-hand panel) compared to staining in villin-cre-RANKL[FL/FL] control mice (left hand panel); sections are counterstained with ToPro3 to detect cell nuclei (grey) and **c** – quantification of staining in the two groups, ** $p = 0.0025$, Mann-Whitney test.
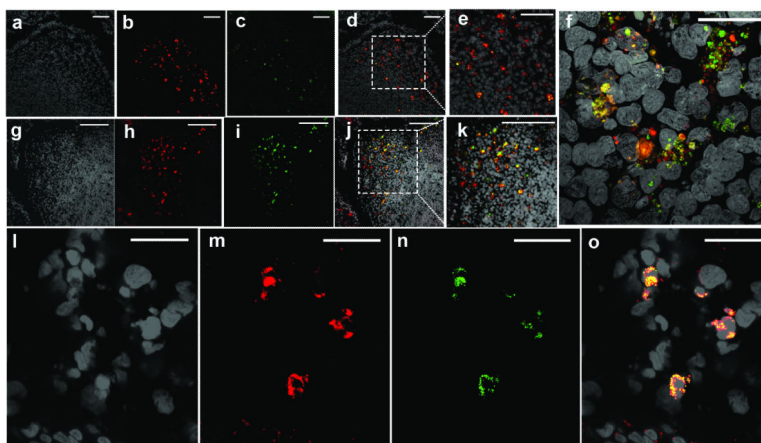
Figure 5. Endogenous nanomineral is co-localised with luminal peptidoglycan and dietary antigen in Peyer's patch (PP) APC

a-k –Mice were fed a normal (a-f) or low (g-k) Ca/P diet plus fluorescently-labelled ovalbumin. **(a-e and g-k)** PP sections were stained with To-Pro-3 for nuclei (grey, images a and g), and with calcein for the endogenous nanomineral (green, images c and i). The fluorescent-labelled ovalbumin (red) is shown in b and h and the overlay of all three stains shows inseparable signals for ovalbumin and the nanomineral in d, e and j, k. Scale bar, 50 μm (a-e) and 100 μm (g-k). **f** – 3D stack, with Huygens Maximum Likelihood Estimation deconvolution, visualised with calcein staining for the endogenous nanomineral (green) and with antibody staining for ovalbumin (red). To-Pro-3 is the nuclear counterstain (grey). Both inseparable co-localisation (orange/yellow) as well as close separation of the protein and mineralised calcium signals are observed, consistent with the partial release of ovalbumin from the nanomineral as it dissolves in the cell lysosome. Scale bar, 20 μm. **l-o** – Human PP sections were stained with To-Pro-3 for nuclei (grey, l), with 2E9 antibody for peptidoglycan (red, m) and calcein for endogenous nanomineral (green, n). The overlay image in o shows the co-localisation of endogenous nanomineral and peptidoglycan implying that the nanomineral transports bacterial peptidoglycan as well as the protein antigen shown above. Scale bars, 25 μm.
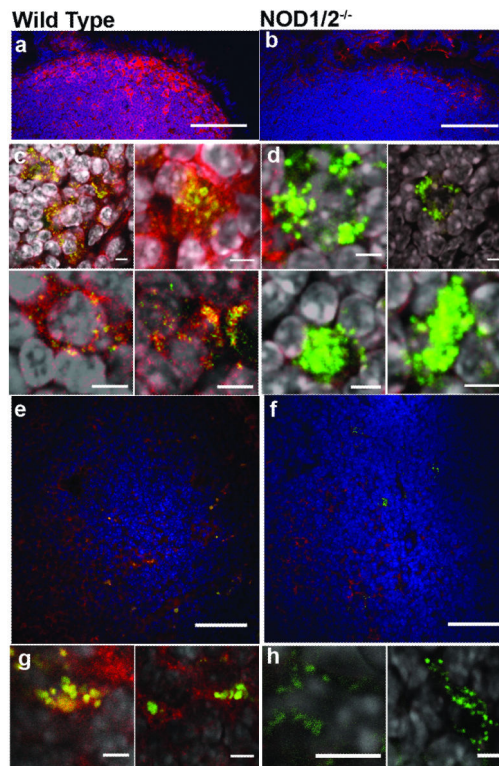
Wild Type **NOD1/2⁻ᐟ⁻**

Figure 6. Peptidoglycan signalling is required for PD-L1 expression on nanomineral-positive APCs of the Peyer's patch sub-epithelial dome and mesenteric lymph nodes

Confocal micrographs showing PD-L1 expression (red) of wild type mice and NOD1/2$^{-/-}$ mice in (a, b) the Peyer's patch, (c, d) representative nanomineral^{+} cells (green) of the Peyer's patch, (e, f) mesenteric lymph nodes (nanomineral in green) and (g, h) representative nanomineral^{+} cells of the mesenteric lymph nodes. Nuclei are shown in blue in low power images (a, b, e and f) and in grey in high power images (c, d g and h). Direct overlap of the green and red appears orange/yellow. Scale bars are 100 μm (a, b), 5 μm (c, d, g and h) and 50 μm (e, f).